Research article

Carbon Future

High performance Li-ion capacitor achieved by rational design of carbon cloth based intercalated anode and porous cathode

Jiang Deng [1]✉, Haiyan Wang[2], and Yong Wang [3]✉

[1] *Innovation Institute of Carbon Neutrality, International Joint Laboratory of Catalytic Chemistry, College of Sciences, Shanghai University, Shanghai 200444, China*
[2] *Key Laboratory of the Ministry of Education for Advanced Catalysis Materials, Department of Chemistry, Zhejiang Normal University, Jinhua 321004, China*
[3] *Advanced Materials and Catalysis Group, Center of Chemistry for Frontier Technologies, State Key Laboratory of Clean Energy Utilization, Institute of Catalysis, Department of Chemistry, Zhejiang University, Hangzhou 310058, China*

Cite This: *Carbon Future* **2025**, *2*, 9200030

Read Online

ABSTRACT: Developing energy storage devices with high energy and power density requires rigorously optimizing both the anode and cathode materials. This work presents a novel approach utilizing commercially available carbon cloth, composed of carbon fibers with a graphitic shell and an amorphous carbon core, as a free-standing electrode for lithium-ion capacitors (LICs). The aligned graphitic layers in the carbon fibers, combined with the three-dimensional structure of the free-standing electrode, reduce tortuosity and enhance power density. To further improve the ion transport kinetics, we employed an $FeCl_3$ pre-insertion strategy, expanding the graphite lattice in the outer shell of the carbon fibers and significantly improving the Li^+ ion diffusion rate, leading to enhanced rate capability. The LICs were fabricated using $FeCl_3$ pre-inserted carbon cloth as a free-standing anode and a porous carbon cloth cathode derived from high-temperature activation. The device achieved an energy density of 5.2 mWh/cm^3 (37.7 Wh/kg), surpassing that of commercial 3.6 V lithium-ion batteries (3.2 mWh/cm^3), with a power density of 6 mW/cm^3. Additionally, the LIC exhibited excellent cycling stability, retaining 86% of its initial capacitance after 10,000 charge–discharge cycles. This study demonstrates a promising strategy for fabricating high-performance and scalable energy storage devices by integrating material design with advanced electrode engineering.

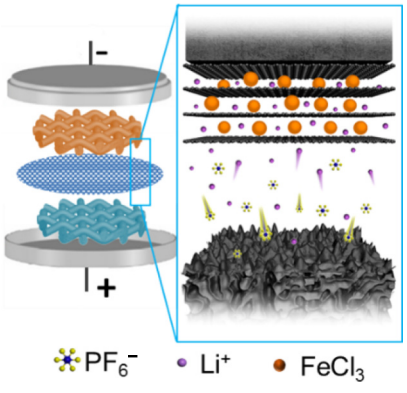

KEYWORDS: Li-ion capacitor, graphite intercalated compounds, porous carbon, free-standing electrode, carbon cloth

1 Introduction

The global shift towards renewable energy sources has introduced new challenges and opportunities in energy storage technologies, particularly within smart grids[1, 2]. The increasing integration of intermittent energy sources, such as solar and wind, into the grid demands energy storage solutions with higher energy and power densities to ensure stable energy supply and efficient grid management[3]. In this regard, lithium-ion capacitors (LICs) have emerged as highly promising hybrid energy storage devices, combining the high-power density of electric double-layer capacitors (EDLCs) with the high energy density of lithium-ion batteries (LIBs)[4–6]. The conventional LIC architecture typically employs activated carbon (AC) as the cathode material, which stores charge electrostatically at the electrode–electrolyte interface through anion adsorption/desorption[7]. Various intercalation compounds are used on the anode side, allowing for the reversible insertion and extraction of lithium ions. However, the non-Faradaic anion adsorption process in the cathode is significantly faster than the Faradaic lithiation process in the anode, creating a kinetic imbalance that limits the overall performance of LICs[8]. Additionally, the energy density of the cathode is generally lower than that of the anode, further exacerbating the energy density mismatch between the two electrodes.

To address these challenges, researchers have explored a variety of strategies, including the development of novel anode materials[9, 10]

Received: October 9, 2024; **Revised:** December 25, 2024
Accepted: December 30, 2024

✉Address correspondence to Jiang Deng, jiangdeng@shu.edu.cn; Yong Wang, chemwy@zju.edu.cn

https://doi.org/10.26599/CF.2025.9200030

and the optimization of electrode architectures[11]. For instance, materials commonly used in lithium-ion batteries, such as graphite[12], transition metal oxides/sulfide[13, 14], and polyanions[3], have been evaluated as anode candidates for LICs. Graphite, in particular, has shown promise for achieving high energy densities, but its lithiation/delithiation kinetics remain a limiting factor, especially at high power densities. Various approaches, such as electrolyte optimization, prelithiation[15], and structural modifications[16], have been employed to enhance the rate capability of graphite-based anodes. However, these improvements often come at the cost of increased complexity and reduced scalability, which are critical considerations for large-scale energy storage applications.

In addition to material selection, the electrode engineering process plays a crucial role in determining the overall performance of LICs[17]. Typically, electrode fabrication involves using binders (e.g., polyvinylidene fluoride (PVDF)) and conductive additives (e.g., acetylene black) to create a slurry cast onto a substrate[18]. While this approach is widely adopted, the use of non-conductive binders and additional additives can negatively impact the energy density and electrochemical performance of the device. Thus, the development of free-standing electrodes with high active material mass loading and without the need for binders or additives presents an attractive solution for next-generation LICs.

In this study, we present a novel approach to LIC design by utilizing carbon cloth (CC) as a free-standing and binder-free electrode material. Carbon cloth, a woven fabric of carbon fibers, offers several advantages, including high electrical conductivity, mechanical flexibility, and the potential for further functionalization. The carbon fibers in CC consist of a graphitic outer layer and an amorphous carbon core, making them a promising candidate for hosting Li^+ ions in LIC anodes. To enhance the ion transport kinetics and improve the rate capability of the graphite layers, we employed a $FeCl_3$ pre-insertion strategy, which expands the graphite lattice and reduces tortuosity, facilitating faster ion diffusion. Additionally, the carbon cloth was activated at high temperatures to introduce a hierarchically porous structure, significantly increasing its surface area and making it suitable for use as a high-capacity cathode. The resulting LIC, assembled with $FeCl_3$-treated carbon cloth (CC_{Fe}) as the anode and activated carbon cloth (ACC) as the cathode, demonstrated exceptional performance, achieving an energy density of 5.2 mWh/cm^3, surpassing that of commercial 3.6 V Li-ion batteries (3.2 mWh/cm^3) at a power density of 6 mW/cm^3. Furthermore, the device exhibited excellent cycling stability, retaining 86% of its initial capacitance after 10,000 charge/discharge cycles. This study not only highlights the potential of functionalized carbon cloth as a dual-role electrode material in LICs but also provides a blueprint for integrating material design with advanced electrode engineering to achieve high-performance energy storage devices. By leveraging the synergistic effects of material innovation and structural optimization, our work offers a new pathway for the development of high-performance and scalable energy storage technologies, addressing the critical challenges faced by the next generation of smart grids and renewable energy systems.

2 Results and discussion

2.1 Fabrication and characterization of CC_{Fe} and ACC

The concept of LICs consists of all CC knitted with the carbon fiber, as presented in **Fig. 1**. $FeCl_3$ was introduced into CC via intercalation reaction under an inert atmosphere, and the obtained CC_{Fe} served as the free-standing anode. Additionally, the CC was activated at 1000 °C to obtain the free-standing cathode for the LICs. The built blocks in the CC are carbon fibers with a core–shell structure in which graphite layers surround the amorphous carbon core (Supplementary Fig. S1). As indicated in the scanning electron microscopy (SEM) image (**Fig. 2**a), the original CC has a smooth surface with a diameter of 5–9 μm. The thickness of the graphitic layer is 5–15 nm, and a lattice space (~ 0.35 nm) between two neighboring (002) planes, as shown in Fig. 2b and Supplementary Fig. S1, corresponds to the graphitic materials. Using three-dimensional (3D) ultra-high resolution X-ray tomography (XRT) (Fig. 2c and Supplementary Fig. S2), the aligned carbon fibers can be visualized[19]. CC_{Fe} was prepared by intercalating $FeCl_3$ into the outer graphitic layers through a solid-phase reaction (see Section 4 for the detailed experimental process). Because of the weak van der Waals interplanar bonding between the graphitic layers, $FeCl_3$ can insert the interplaner and expand the lattice distance at elevated temperatures. When intercalated with $FeCl_3$, the smooth surface (Fig. 2d) of the CC_{Fe} and aligned structure (Fig. 2f) are still maintained, but a bright circle around the carbon fiber can be observed through SEM image (Fig. 2d). The reason for this phenomenon might be that higher conductivity (Supplementary

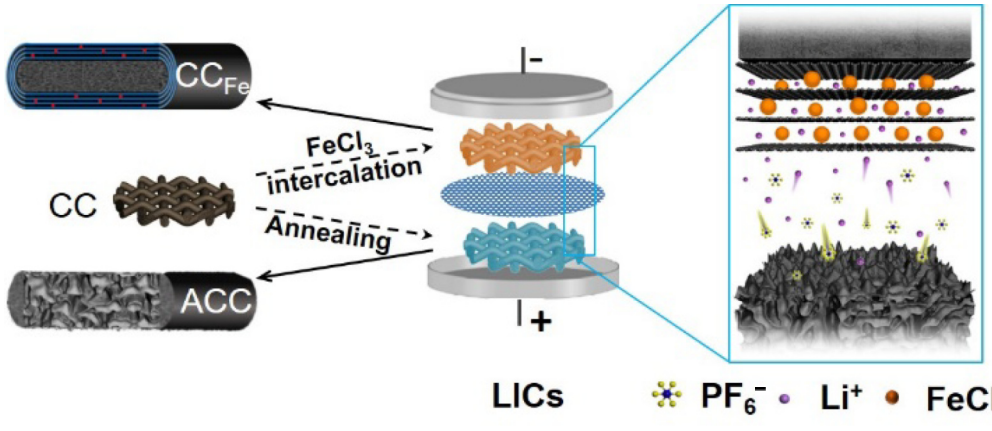

Fig. 1. Schematic diagram of LICs assembling. Fabrication of LICs by using ACC as cathode and CC_{Fe} as the anode and the mechanism of LICs fabricated here during charging (the separator is neglected in highlighting the dynamic processes).

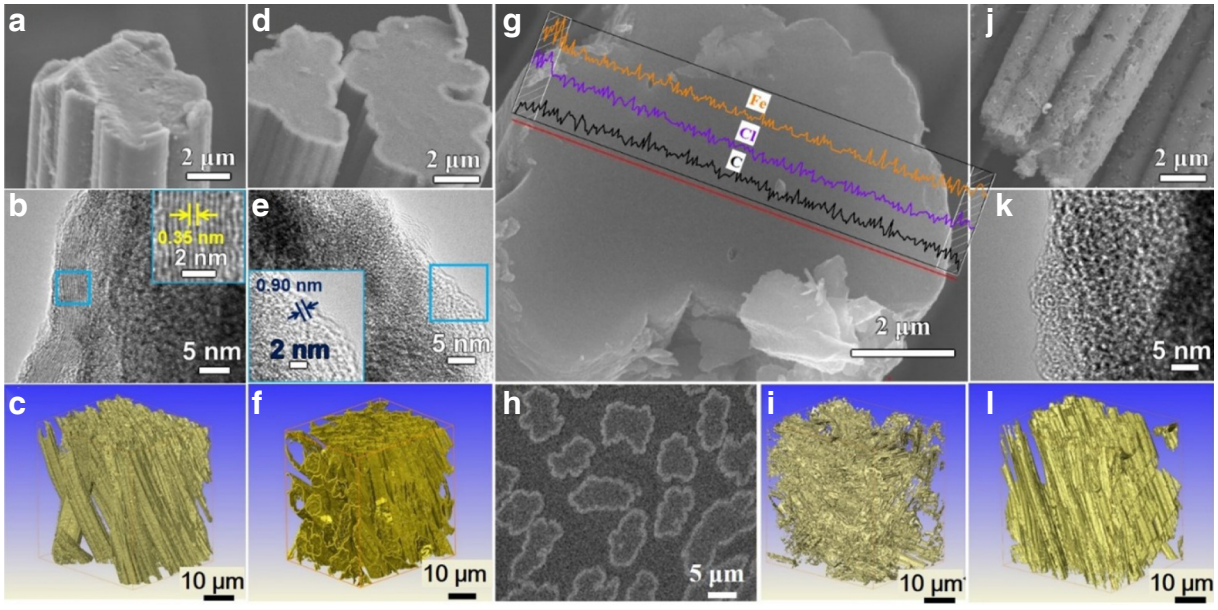

Fig. 2. Structure characterization of CC-based materials. **a**, SEM image, **b**, HRTEM image, and **c**, 3D XRT image of CC. **d**, SEM image, **e**, HRTEM image, and **f**, 3D XRT image of CC_{Fe}. **g**, Cross-section SEM image and EDX profile of CC_{Fe}. **h**, Absorption contrast two-dimensional (2D) reconstructed tomographic slice of CC_{Fe}. **i**, 3D XRT image of PCC. **j**, SEM image, **k**, HRTEM image, and **l**, 3D XRT image of ACC. These results indicate that the porous structure has been introduced successfully into the carbon cloth, and the lattice of graphite shell has been expended by the $FeCl_3$. The three-dimensional free-standing structures of CC (c), CC_{Fe} (f), and ACC (l) still maintain while the PCC (i) shows disordered and tortuously structure.

Fig. S3) of the intercalated outer layer leads to stronger electron scattering. The increase in conductivity for graphite intercalation compounds primarily stems from the injection of additional charge carriers into the graphite layers through the intercalation process, which leverages the high in-plane mobility of graphite to enhance electrical conduction[20]. A similar phenomenon was also observed in XRT measurement (Fig. 2h), in which the bright circle suggested a stronger X-ray adsorption from $FeCl_3$. With $FeCl_3$ intercalation, the lattice distance increased by 0.9, 0.6, and 0.45 nm, corresponding to stage-1 or diluted stage-1 graphite intercalation compounds[21, 22] based on a high-resolution transmission electron microscopy (HRTEM) image (Fig. 2e and Supplementary Fig. S4). The outer layer exhibited larger distance because it contacted with $FeCl_3$ thoroughly. The existence of $FeCl_3$ in CC_{Fe} was further confirmed by an energy dispersive X-ray spectroscopy (EDS) combined with SEM (Supplementary Figs. S5 and S6). The obvious Kα signals of C, Cl, and Fe can be seen from Supplementary Fig. S5b and the atomic ratio of Cl/Fe is 4.4:1 (Supplementary Table S1), as the extra Cl might derived from partial hydrolysis of $FeCl_3$. To investigate the distribution of $FeCl_3$ in the carbon fiber, the SEM-EDS line scan was conducted, as indicated in Fig. 2g. Fe and Cl distribute in the outer layer of the carbon fiber, which confirms $FeCl_3$ intercalation into the graphite layer of carbon fiber. However, the $FeCl_3$ might be an amorphous structure, as no diffraction peak corresponding to $FeCl_3$ is observed. These results showed that $FeCl_3$ intercalated into carbon fiber successfully, resulting in the expended lattice.

As reported previously, CC can be simply modified by high-temperature annealing process giving rise to plentifully porous structure in ACC[23]. The original carbon fiber has been etched during the elevated temperature annealing process, resulting in rather rough surface and macroporous structure of ACC (Fig. 2j and Supplementary Fig. S7). Additionally, the graphitic layer becomes disordered and plenty of micropores have been included in ACC (Fig. 2k). Although the surface of carbon fiber became rough, the aligned structure of ACC still maintained according to 3D XRT image of ACC (Fig. 2l and Supplementary Fig. S8). The precise pore structure of ACC was characterized by N_2 sorption. N_2 adsorption/desorption isotherm (Supplementary Fig. S9a and Table S2) shows that micropore filling occurs at the low-pressure region and H4 hysteresis loop between 0.5 and 1 (P/P_0) indicated coupling mesopores and macropores. The pore size distribution based on density functional theory (DFT) further confirms the existence of macro-, meso-, and micropore, and the most probable pore sizes are 1 and 2.5 nm (Supplementary Fig. S9b). The hierarchically porous structure of ACC is favorable for fast ion diffusion and effective ion adsorption[24]. High-temperature annealing process introduced more defects, as suggested by Raman spectra (Supplementary Fig. S9c), with the intensity ratio of D-band to G-band increasing from 1.2 to 1.3. Although the graphitic outer layers became disordered, there are negligible changes in the X-ray diffraction (XRD) pattern (Supplementary Fig. S9d) because of the dominant amorphous carbon. These results indicate that high-temperature activation successfully introduces a plentiful porous structure while maintaining the CC macrostructure.

2.2 The merits of free-standing electrode

To evaluate the importance of free-standing property, CC was cut and ground into power and then was fabricated as electrode by adding PVDF and carbon black. The as-obtained electrode was labelled as PCC whose disorganized structure was presented in Fig. 2i and Supplementary Fig. S10. The SEM image of PCC (Supplementary Fig. S11) also shows that the broken carbon fibers mishmash each other and the binder and carbon black adhere to the broken blocks. The electrochemical performances of PCC, ACC, and CC_{Fe} were evaluated through cycle voltammetry (CV) tests in a confined coin cell with Li foil as the counter electrode and reference electrode in 1 M $LiPF_6$ ethylene carbonate (EC)/dimethyl carbonate (DMC)/diethyl carbonate (DEC) (1:1:1). CC_{Fe} served as

the anode and the operation voltage window was set as 0.01–3 V at a scan rate of 0.1 mV/s. A typical cyclic voltammogram for the graphite materials was observed for CC, PCC, and CC_{Fe}, as shown in Fig. 3a[25]. The two small irreversible peaks at 0.25 and 0.75 V versus Li^+/Li can be attributed to the intercalation of Li^+ to graphite. No redox peaks correspond to the $FeCl_3$, which might be attributed to the inadequate amount of $FeCl_3$. The extra capacity of CC_{Fe} and PCC might be attributed to larger electric adsorption because of their larger surface areas (Supplementary Table S2) and the additives of carbon black, respectively. While the large surface area of the cathode is favorable for the adsorption of PF_6^- and gives rise to larger EDLC than CC (Fig. 3b). The EDLC also enables the ACC//Li with good rate performance, where the capacitance decreases from 792 to 480 mF/cm^2 when the current density increased by 20 times (Supplementary Fig. S12).

2.3 The capacity and ion transport kinetics of CC_{Fe}

To probe the effect of structural features on the ion transport kinetics, electrochemical impedance spectroscopy (EIS) measurements were conducted on samples by using a symmetric cell with two identical electrodes (Supplementary Fig. S13a). The EIS based on symmetric cell can provide more accurate impedance spectra of the electrode–electrolyte interface than the traditional one with counter electrode. A non-Faradaic process with a state of charge (SOC) at 0% can be obtained through the Nyquist plots (Fig. 3c) before lithiation[26]. The plot of CC_{Fe} exhibit a 45° slope in the frequency region between 4 and 628 Hz and quasi-vertical lines at lower frequency (< 1.6 Hz) which indicate non-Faradaic process. A transmission line model (TLM) was used for further validated analysis based on the EIS profiles (Supplementary Figs. S13b and S13c). The projection defined as $R_{ion}/3$ based on TLM simulation reflects the ionic resistance for the electrolyte filled pores or lattice inside the electrode. The determination of $R_{ion}/3$ for each composite electrode is shown in Fig. 3d, which was calculated based on the Warburg element open circuit terminus (W_o) (Supplementary Fig. S14 and Table S3). CC_{Fe} shows a smaller R_{ion} (33 Ω/cm^2) than CC (1072 Ω/cm^2), which indicates improved ion transport kinetics. This contribution (R_{high}, Supplementary Fig. S15) raised from an interfacial charge transfer resistance of the electrode reveals that the graphite layer, especially the $FeCl_3$ intercalated one, accelerated the charge transfer of the interface between the electrolyte and electrode. Moreover, R_{sol}, another parameter derived from the TLM, is in line with the resistance of the electrode. (Supplementary Fig. S15). The CC_{Fe} with expanding lattice and the three-dimensional

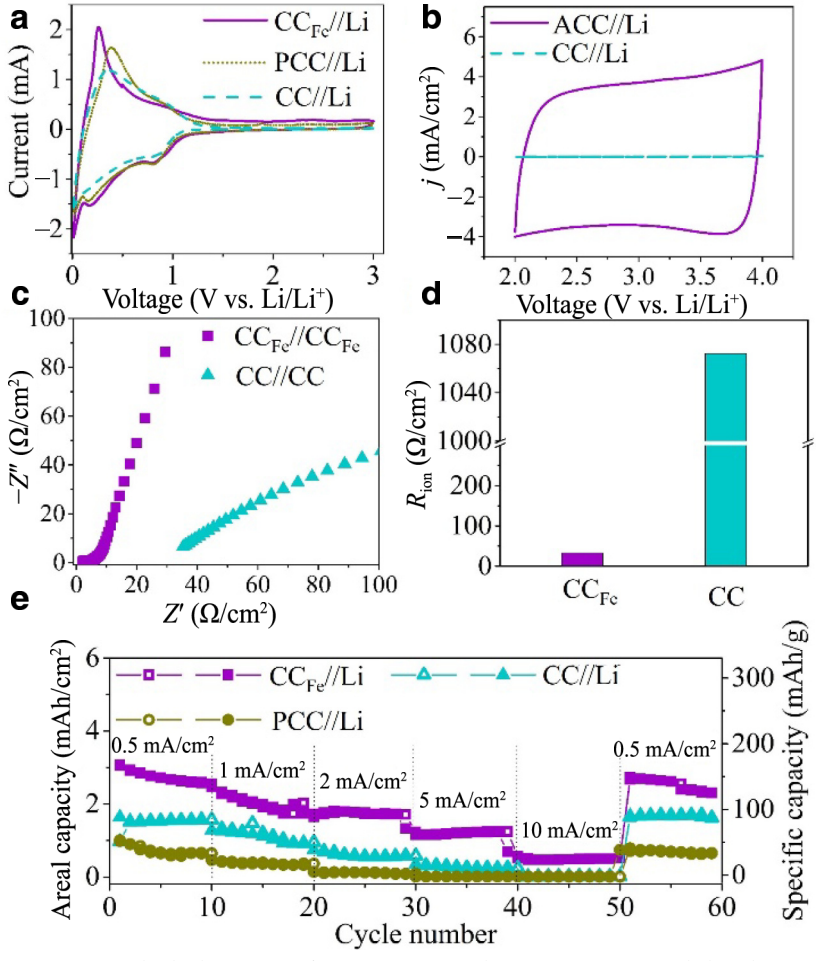

Fig. 3. Electronic performance of half-cell. **a**, **b**, The third CV curves of CC_{Fe}//Li, CC//Li, and PCC//Li at 0.1 mV/s with the voltage window from 0.01 to 3 V vs. Li/Li^+ (a), and ACC//Li and CC//Li at 5 mV/s with voltage window from 2 to 4 V vs. Li/Li^+ (b). **c**, Nyquist plots obtained from potentiostatic EIS of a symmetric cell using two identical electrodes with a state of charge at 0%. **d**, R_{ion} determined from transmission line mode simulation. **e**, Specific capacities of CC_{Fe}//Li, CC//Li, and PCC//Li normalized by geometry surface areas at various rates. These results indicated that CC_{Fe} with free-standing structure and expanded lattices show higher capacity and faster ion diffusion kinetics.

framework is favorable for the Li-ion diffusion and insertion/desertion. The specific capacity of CC_{Fe} is 160 mAh/g at 0.5 mA/cm^2, which is lower than the theoretical number. It is still hard to fully use the electrode materials as the extensive mass loading (~ 20 mg). The specific capacity of CC_{Fe} is 2.7 mAh/cm^2 at 0.5 mA/cm^2, which is higher than pristine CC (1.5 mAh/cm^2) and PCC (0.8 mAh/cm^2). When the current density increased by 5 mA/cm^2, the capacity of CC//Li is 0.3 mAh/cm^2, while there is almost no capacity for PCC. These results demonstrate that free-standing CC with aligned graphite shows better intercalation capacity than PCC. The rate capability of CC_{Fe} was further improved, and the capacity was 0.5 mAh/cm^2, which is 25 times larger than CC//Li. The cyclability of Li-ion battery-based graphite is inferior because of the degradation during the Li-ion insertion/desertion. As other preinsertion materials indicate, cyclability can be improved because the extended lattice can buffer the volume change during the insertion/desertion process[27]. As shown in Supplementary Fig. S16, the capacity maintains 56% (1.0 mAh/cm^2) for CC_{Fe}//Li, which is higher than 39% (0.34 mAh/cm^2) of CC//Li after 100 charge–discharge processes.

2.4 The performance of assembled device

Li-ion capacitors, by using battery material as an anode and electronic double-layer capacitor material as a cathode, can bridge the gap between the battery and electrochemistry capacitor. The performance of the assembled devices coupling CC_{Fe} as anode and ACC as cathode (CC_{Fe}//ACC) was determined through CV and galvanostatic charge–discharge (GCD) measurements. Before assembling, CC_{Fe} was under lithiation by assembling with Li foil in 1 M $LiPF_6$ EC/DMC/DEC (Supplementary Fig. S17) and discharged to 0.1 V vs. Li/Li$^+$ at 0.5 mA/cm^2. For comparison, CC_{Fe}//CC and CC//ACC were also assembled. As is shown in Fig. 4a, CC_{Fe}//ACC (1390 mF/cm^2) shows higher capacitance than that of CC//ACC (1025 mF/cm^2) at 5 mV/s. In particular, the capacitance of CC_{Fe}//ACC still maintains 529 mF/cm^2 when the scan rate increases to 50 mV/s, which is better than that of CC//ACC (232 mF/cm^2). These results demonstrate the expanding lattice is better than the Li-ion diffusion and insertion. The specific capacitance of CC_{Fe}//ACC is 780 mF/cm^2, which is higher than that of CC//ACC (630 mF/cm^2) at 0.5 mA/cm^2 (Fig. 4c and Supplementary Fig. S18). When the current density was set at 10 mA/cm^2, CC_{Fe}//ACC exhibited a capacitance of 580 mF/cm^2, 9 times that of CC//ACC (65 mF/cm^2) (Fig. 4c and Supplementary Fig. S17). For practical use, a fast charge and slow discharge process are favorable. Then, the performance of the devices was charged at 10 mA/cm^2 and discharged at 0.5 mA/cm^2. As indicated in Fig. 4d, the capacitance of CC_{Fe}//ACC is 412 mF/cm^2 based on the discharge, which is ~ 3 times that of CC//ACC (158 mF/cm^2). The

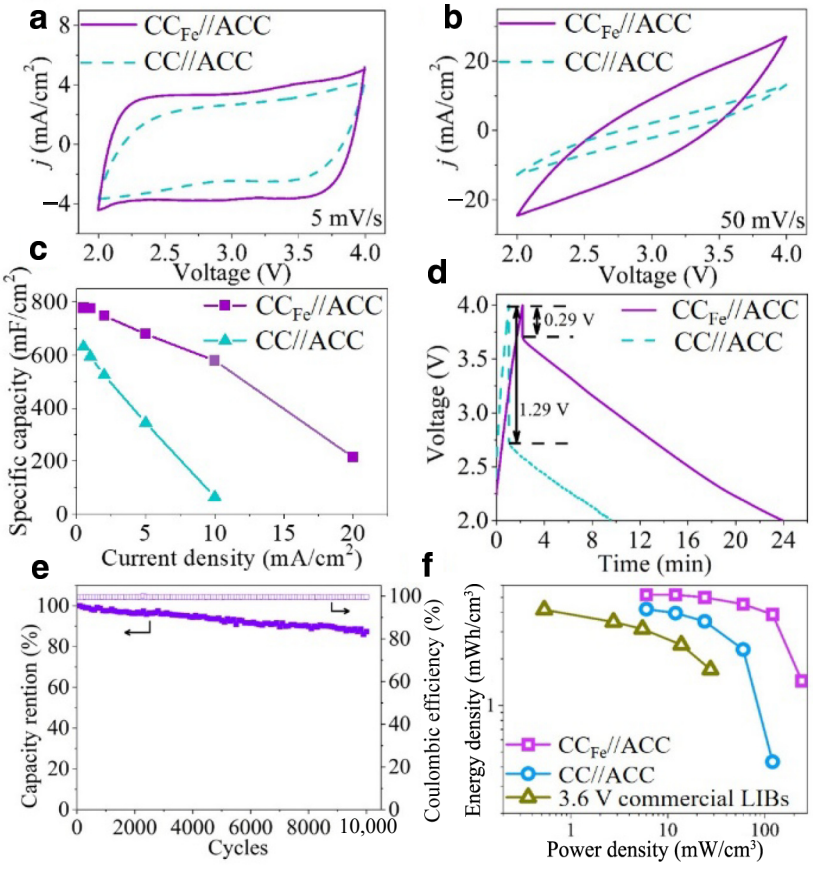

Fig. 4. Electronic performance of full-cell. **a**, **b**, CV curves of CC_{Fe}//ACC, CC//ACC, and CC//CC at 5 mV/s (a) and 50 mV/s (b) from 2.0 to 4.0 V. **c**, Specific capacitance of CC_{Fe}//ACC and CC//ACC at various rates. **d**, GCD curves of CC_{Fe}//ACC and CC//ACC charged by 10 mA/cm^2 and discharged by 1 mA/cm^2. **e**, Durability and Coulombic efficiency of CC_{Fe}//ACC tested at 10 mA/cm^2. **f**, Ragone plot of CC_{Fe}//ACC, CC//ACC, and 3.6 V commercial Li-ion battery normalized by volume. These results suggested that the assemble device combining ACC and CC_{Fe} showed high performance towards capacity and ratability which is even better than 3.6 V commercial Li-ion battery.

smaller *IR*-drop (0.29 V vs. 1.29 V) of CC_{Fe}//ACC in Fig. 4d can be ascribed to the lower R_s (Supplementary Fig. S19). Also, the steeper Nyquist plot in the low frequency of CC_{Fe}//ACC compared with CC//ACC indicates its fast diffusion kinetic process (Supplementary Fig. S19). The cyclability of CC_{Fe}//ACC was tested through GCD at 10 mA/cm^2. As shown in Fig. 4e, the retention of CC_{Fe}//ACC is 87% after 10,000 charge–discharge process.

As mentioned above, Li-capacitor coupling expanding anode with porous cathode shows high capacitance, good rate capability, and excellent cycling stability. Energy density and power density based on the geometry surface and volume of the whole device are more meaningful parameters for evaluating the performance of devices. A Ragone plot (Fig. 4f and Supplementary Fig. S20) shows the device's and commercial storage battery's mass and volumetric performance. Volumetric energy density (E_v) of CC_{Fe}//ACC reaches 5.2 mWh/cm^3 (at volumetric power density (P_v) of 6 mW/cm^3) which is higher than CC//ACC (4.2 mWh/cm^3 at 6 mW/cm^3) and 3.6 V commercial Li-ion battery (Supplementary Fig. S21) (2.7 mWh/cm^3 at 4.9 mW/cm^3). These values maintain 3.89 mWh/cm^3 at 120 mW/cm^3, which is 10-fold higher than that of CC//ACC.

3 Conclusions

In summary, the graphitic outer layer of carbon cloth was expended through $FeCl_3$-intercalation, which is favorable for Li-ion insertion/desertion and shows better rate capability. An elevated temperature annealing process endows carbon clothes with hierarchically porous structures suitable for electrolyte diffusion and ion adsorption. A high-performance Li-ion capacitor was achieved by combining the expending anode and porous cathode. The aligned graphitic shell and the expended graphitic layer can reduce the tortuosity and facilitate the Li-ion insertion/desertion kinetics. With that, the as-assembled device gives an energy density of 1.44 mWh/cm^3 at a power density of 241 mW/cm^3, which is better than the commercial Li-ion coin cell and fills in the gap between the supercapacitor and Li-ion battery. This strategy provides an innovative idea for fabricating high-performance Li-ion capacitors by combining materials design and electrode engineering.

4 Experimental

4.1 Preparation of ACC

ACC was prepared according to the method reported in our previous work[28]. Briefly, a piece of commercial CC (4 cm × 4 cm) was cleaned with ethanol and ultrapure (UP) water and then dried at a 70 °C in the oven. Subsequently, the cleaned CC was annealed at 1000 °C for 1 h with 5 °C/min in industry nitrogen (99% purity) flow. The resultants were cleaned with UP water and resulted in ACC. The weight of ACC was 22.5 mg, and the thickness was about 0.38 mm.

4.2 Synthesis of CC_{Fe}

CC intercalation with $FeCl_3$ (CC_{Fe}) was synthesized through a solid-phase reaction. Commercial CC was tailored into circular pieces with a diameter of 14 mm. Then, the tailored CC and 1.0 g of anhydrous $FeCl_3$ were put into weighing bottle (25 mm × 40 mm) and sealed in the Ar-purged glove box. The bottle was put into a sealed stainless-steel pot and underwent a high-temperature annealing (470 °C) with 5 °C/min for 24 h. The post-CC was washed with UP water and 0.1 M HCl, resulting in CC_{Fe} after drying at 70 °C in the oven. The weight of the as-obtained CC_{Fe} was 20 mg, and the thickness was about 0.35 mm.

4.3 Fabrication of PCC

Commercial CC was tailored into circular pieces with a diameter of 14 mm. Then, the tailored CC was cut into small pieces and ground into power. 1 mg of PVDF and 1 mg of carbon black were added to the CC powder. N-methyl-2-pyrrolidone (NMP) was added to make slurry. The PCC was fabricated by using Al foil as support and a mode with a diameter of 14 mm was used to control the size of electrode. After dried in 120 °C overnight, the PCC was obtained.

4.4 Prelithiation of CC_{Fe}

CC_{Fe} and a piece of Li foil were sealed in a coin cell (2025) in the presence of a separator, with 1 M $LiPF_6$ dissolved in a 1:1:1 (v:v:v) mixture of EC, DEC, and DMC as the electrolytes. Then, the cell underwent discharge with a current density of 0.5 mA/cm^2 and a terminal voltage of 0.1 V.

4.5 Assembly of half-cells and LICs

Half cells were assembled to measure the electrochemical performances of ACC and CC_{Fe}, respectively, in which lithium metal foil was used as the counter and reference electrode and 1 M $LiPF_6$ dissolved in 1:1:1 (v:v:v) mixture of EC, DMC, and DEC was employed as the electrolyte. LICs were also assembled in coin cells (2025) with prelithiation CC_{Fe} negative and ACC positive electrodes in the same electrolyte.

4.6 Material characterization

Morphological information and energy-dispersive X-ray (EDX) spectra were obtained using field emission scanning electron microscopy (FESEM, SU-8010) at an acceleration voltage of 5 KV for regular measurement and 20 KV for the EDX test. HRTEM was performed on JEM 2100F with an acceleration voltage of 300 KV. The Raman spectra were collected through JY, HR 800, using 514 nm laser excitation at room temperature. The porous structure was characterized by N_2 sorption analysis at 77 K using a Micromeritics ASAP 2020. The specific surface area (SSA) was calculated by Brunauer–Emmette–Teller (BET) method, and the pore size distribution (PSD) was recorded by density functional theory pore mode. XRT was performed on Carl Zeiss Xradia 800 Ultra using both absorption and phase contrast modes. The pixel size was about 64 nm. The image was 3D visualized using Avizo fire software.

4.7 Electrochemical tests

CV was performed at different scanning rates with the desired window in Gamry Reference 600 potentiostat. EIS was carried out through Gamry Reference 600 at the open circuit voltage from 100 KHz to 0.01 Hz and an alternating current signal with an amplitude of 10 mV as the perturbation. Galvanostatic charge/discharge tests were performed under a LAND-CT2001 instrument at ambient temperature.

4.8 Calculations

For half-cell configuration, the surface specific capacity (C) was calculated according to the galvanostatic discharge–charge curve using Eq. (1)

$$C\ (\mathrm{mAh/cm^2}) = \frac{I \times \Delta t}{3600 \times S} \quad (1)$$

where I (mA) is the constant current, Δt (s) is the discharge time, and S (cm^2) is the geometric surface area of carbon cloth.

For a device measurements, surface specific capacitance (C_s) was calculated as

$$C_s\ (\mathrm{mF/cm^2}) = \frac{I \times \Delta t}{S \times U} \quad (2)$$

where I (mA) is the constant current, Δt (s) is the discharge time, S (cm^2) is the geometric surface area of carbon cloth, and U (V) is the potential window.

For the CV curves, surface specific capacitance (C_s) was calculated as

$$C_s\ (\mathrm{mF/cm^2}) = \frac{\int I \mathrm{d}U}{\nu S U} \quad (3)$$

where I (mA) is current, ν (V/s) is the potential scan rate, S (cm^2) is the geometric surface area of carbon cloth, and U (V) is the potential window.

E_v was calculated as

$$E_v = \frac{\int IU\mathrm{d}t}{V} \quad (4)$$

where I (A) is the discharge current, U is the potential, and V is the assembly device volume. P_v was calculated as

$$P_v = \frac{E_v}{\Delta t} \quad (5)$$

where Δt is the discharge time.

References

[1] Yang, J.; Li, M. Z.; Fang, S. L.; Wang, Y. L.; He, H. Y.; Wang, C. L.; Zhang, Z. J.; Yuan, B. C.; Jiang, L.; Baughman, R. H. et al. Water-induced strong isotropic MXene-bridged graphene sheets for electrochemical energy storage. *Science* **2024**, *383*, 771–777.

[2] Zhang, M.; Lan, S.; Yang, B. B.; Pan, H.; Liu, Y. Q.; Zhang, Q. H.; Qi, J. L.; Chen, D.; Su, H.; Yi, D. et al. Ultrahigh energy storage in high-entropy ceramic capacitors with polymorphic relaxor phase. *Science* **2024**, *384*, 185–189.

[3] Xu, X. Y.; Zhang, J.; Zhang, Z. H.; Lu, G. D.; Cao, W.; Wang, N.; Xia, Y. M.; Feng, Q. L.; Qiao, S. L. All-covalent organic framework nanofilms assembled lithium-ion capacitor to solve the imbalanced charge storage kinetics. *Nano-Micro Lett.* **2024**, *16*, 116.

[4] Bi, R. Y.; Xu, N.; Ren, H.; Yang, N. L.; Sun, Y. G.; Cao, A. M.; Yu, R. B.; Wang, D. A hollow multi-shelled structure for charge transport and active sites in lithium-ion capacitors. *Angew. Chem., Int. Ed.* **2020**, *59*, 4865–4868.

[5] Liang, J. X.; Wang, D. W. Design rationale and device configuration of lithium-ion capacitors. *Adv. Energy Mater.* **2022**, *12*, 2200920.

[6] Wang, L.; Zhang, X.; Kong, Y. Y.; Li, C.; An, Y. B.; Sun, X. Z.; Wang, K.; Ma, Y. W. Metal-organic framework-derived $CoSe_2$@N-doped carbon nanocubes for high-performance lithium-ion capacitors. *Rare Met.* **2024**, *43*, 2150–2160.

[7] Parejo-Tovar, A.; Merlet, C.; Ratajczak, P.; Béguin, F. *Operando* tracking of ion population changes in the EDL electrode of a lithium-ion capacitor during its charge/discharge. *Energy Storage Mater.* **2024**, *73*, 103810.

[8] Ma, Y. B.; Wang, K.; Xu, Y. N.; Zhang, X. D.; Peng, Q. F.; Guo, Y.; Sun, X. Z.; Zhang, X.; Wu, Z. S.; Ma, Y. M. Black phosphorus covalent bonded by metallic antimony toward high-energy lithium-ion capacitors. *Adv. Energy Mater.* **2024**, *14*, 2304408.

[9] Gao, Y.; Tang, Y. K.; Liu, L.; Li, X. H.; Qian, M.; Ma, W. J. A Novel anode material Li_2FeGeO_4 with lithium storage mechanism controlled by both iron and germanium elements. *Small* **2023**, *19*, 2304593.

[10] Guo, X. Y.; Qiao, Y.; Yi, Z. L.; Pedersen, C. M.; Wang, Y. X.; Tian, X. D.; Han, P. D. Furfural residues derived nitrogen-sulfur co-doped sheet-like carbon: An excellent electrode for dual carbon lithium-ion capacitors. *Green Energy Environ.* **2024**, *9*, 1427–1439.

[11] Liang, T.; Mao, Z. F.; Li, L. Y.; Wang, R.; He, B. B.; Gong, Y. S.; Jin, J.; Yan, C. J.; Wang, H. W. A mechanically flexible necklace-like architecture for achieving fast charging and high capacity in advanced lithium-ion capacitors. *Small* **2022**, *18*, 2201792.

[12] Peng, Q. F.; Wang, K.; Gong, Y.; Zhang, X. D.; Xu, Y. N.; Ma, Y. B.; Zhang, X.; Sun, X. Z.; Ma, Y. W. Tailoring lignin-derived porous carbon toward high-energy lithium-ion capacitor through varying sp^2- and sp^3-hybridized bonding. *Adv. Funct. Mater.* **2023**, *33*, 2308284.

[13] Zhu, C. Y.; Mao, J. J.; Zhao, J. Y.; Luo, Y. H.; Li, J. D.; Lei, C.; Li, G.; Cheng, F. A facile *in situ* sulfurization strategy for heterostructured SnS_2@graphene scrolls anode with enhanced initial coulombic efficiency for high-energy lithium storage. *Adv Funct. Mater.* **2024**, 2406730.

[14] Zhao, C. Y.; Yao, S. Y.; Li, C.; An, Y. B.; Zhao, S. S.; Sun, X. Z.; Wang, K.; Zhang, X.; Ma, Y. W. Recent advances in transition metal oxides as anode materials for high-performance lithium-ion capacitors. *Chem. Eng. J.* **2024**, *497*, 154535.

[15] Sun, C. K.; Zhang, X.; Li, C.; Wang, K.; Sun, X. Z.; Ma, Y. W. High-efficiency sacrificial prelithiation of lithium-ion capacitors with superior energy-storage performance. *Energy Storage Mater.* **2020**, *24*, 160–166.

[16] Li, G. C.; Huang, Y. L.; Yin, Z. L.; Guo, H. J.; Liu, Y.; Cheng, H.; Wu, Y. P.; Ji, X. B.; Wang, J. X. Defective synergy of 2D graphitic carbon nanosheets promotes lithium-ion capacitors performance. *Energy Storage Mater.* **2020**, *24*, 304–311.

[17] Zhang, Y. Z.; Hu, Z. W.; Li, H. W.; Qiao, J. Q.; Wang, X. J.; Liu, Z. M. A conductive flexible carbon nanoyarns embedded with VN quantum dots for highly kinetics-compatible Li-ion capacitors. *Chem. Eng. J.* **2024**, *492*, 152221.

[18] Lv, C.; He, W. J.; Jiang, J. M.; Zhen, E. M.; Dou, H.; Zhang, X. G. Structure optimization of solvent-free $Li_4Ti_5O_{12}$ electrodes by electrostatic spraying for lithium-ion capacitors. *J. Power Sources* **2023**, *556*, 232487.

[19] Wang, S. G.; Wang, S. C.; Zhang, L. Application of high resolution transmission X-ray tomography in material science. *Acta Metall. Sin.* **2013**, *49*, 897.

[20] Dresselhaus, M. S.; Dresselhaus, G. Intercalation compounds of graphite. *Adv. Phys.* **1981**, *30*, 139–326.

[21] Matsumoto, R.; Okabe, Y. Electrical conductivity and air stability of $FeCl_3$, $CuCl_2$, $MoCl_5$, and $SbCl_5$ graphite intercalation compounds prepared from flexible graphite sheets. *Synth. Met.* **2016**, *212*, 62–68.

[22] Wang, F.; Yi, J.; Wang, Y. G.; Wang, C. X.; Wang, J. Q.; Xia, Y. Y. Graphite intercalation compounds (GICs): A new type of promising anode material for lithium-ion batteries. *Adv. Energy Mater.* **2014**, *4*, 1300600.

[23] Wang, H. Y.; Fan, R. X.; Miao, J. Y.; Deng, J.; Wang, Y. Oxygen groups immobilized on micropores for enhancing the pseudocapacitance. *ACS Sustainable Chem. Eng.* **2019**, *7*, 11407–11414.

[24] Deng, J.; Xiong, T. Y.; Xu, F.; Li, M. M.; Han, C. L.; Gong, Y. T.; Wang, H. Y.; Wang, Y. Inspired by bread leavening: One-pot synthesis of hierarchically porous carbon for supercapacitors. *Green Chem.* **2015**, *17*, 4053–4060.

[25] Zhang, J.; Shi, Z. Q.; Wang, C. Y. Effect of pre-lithiation degrees of mesocarbon microbeads anode on the electrochemical performance of lithium-ion capacitors. *Electrochim. Acta* **2014**, *125*, 22–28.

[26] Sun, H. T.; Mei, L.; Liang, J. F.; Zhao, Z. P.; Lee, C.; Fei, H. L.; Ding, M. N.; Lau, J.; Li, M. F.; Wang, C. et al. Three-dimensional holey-graphene/niobia composite architectures for ultrahigh-rate energy storage. *Science* **2017**, *356*, 599–604.

[27] Dong, Y. F.; Xu, X. M.; Li, S.; Han, C. H.; Zhao, K. N.; Zhang, L.; Niu, C. J.; Huang, Z.; Mai, L. Inhibiting effect of Na^+ pre-intercalation in MoO_3 nanobelts with enhanced electrochemical performance. *Nano Energy* **2015**, *15*, 145–152.

[28] Wang, H. Y.; Deng, J.; Xu, C. M.; Chen, Y. Q.; Xu, F.; Wang, J.; Wang, Y. Ultramicroporous carbon cloth for flexible energy storage with high areal capacitance. *Energy Storage Mater.* **2017**, *7*, 216–221.

Data availability

All data needed to support the conclusions in the paper are presented in the manuscript and the Supplementary Information. Additional data related to this paper may be requested from the corresponding author upon request.

Acknowledgements

This work was financially supported by the National Natural Science Foundation of China (Nos. 22476121, 22325204, 22302177), Shanghai Pujiang Programme (No. 24PJD033), and the Key Science and Technology Project of Jinhua City (No. 2024-1-004).

Author contributions

J. D. conducted the experiments, collected the data, and wrote the manuscript. H. W. assisted with the XRT characterization. Y. W. conceived and planned the project, supervised the experimental work, and revised the manuscript.

Competing interests

The authors have no competing interests to declare that are relevant to this article.

Use of AI statement

None.

Additional information

Supplementary Information The online version contains supplementary material available at https://doi.org/10.26599/CF.2025.9200030.